Communications Chemistry

https://doi.org/10.1038/s42004-026-01896-w

Article in Press

Hydrogen-assisted dehydrochlorination of 1,1,1,2-tetrafluoro-2-chloropropane to 2,3,3,3-tetrafluoropropene over Pd-Ag/nano-MgF_2 with optimized Pd isolated sites

Received: 9 May 2025

Accepted: 8 January 2026

Cite this article as: Yang, C., Mao, W., Dong, X. *et al.* Hydrogen-assisted dehydrochlorination of 1,1,1,2-tetrafluoro-2-chloropropane to 2,3,3,3-tetrafluoropropene over Pd-Ag/nano-MgF_2 with optimized Pd isolated sites. *Commun Chem* (2026). https://doi.org/10.1038/s42004-026-01896-w

Chen Yang, Wei Mao, Xingzong Dong, Song Tian, Jinni Shen, Wei Zhang, Zhaotie Liu, Jian Lu & Erhard Kemnitz

Hydrogen-assisted dehydrochlorination of 1,1,1,2-tetrafluoro-2-chloropropane to 2,3,3,3-tetrafluoropropene over Pd-Ag/nano-MgF_2 with optimized Pd isolated sites

Chen Yang[1,2], Wei Mao[2,*], Xingzong Dong[2], Song Tian[2], Jinni Shen[3], Wei Zhang[2], Zhaotie Liu[1], Jian Lu[2,*], Erhard Kemnitz[4]

[1]College of Chemistry and Chemical Engineering, Shaanxi University of Science and Technology, Xi'an 710021, China

[2]State Key Laboratory of Fluorine & Nitrogen Chemical, Xi'an Modern Chemistry Research Institute, Xi'an 710065, China.

[3]Research Institute of Photocatalysis, College of Chemistry, Fuzhou University, Fuzhou, 350116, China.

[4]Department of Chemistry, Humboldt-Universitat zu Berlin, Brook-Taylor-Strase 2, D-12489 Berlin, Germany.

*Corresponding author.

E-mail: hz_mw@163.com; lujian204@gmail.com

Abstract

Hydrogen-assisted dehydrochlorination process (HaDHC) is an attractive route for the production of fluorine-containing olefins under relatively mild conditions, so far lacking the highly efficient metal-based catalysts and their design strategy. Here we report a nano-MgF_2 supported Pd-Ag catalyst with a tunable Pd dispersion, which is optimized by the Pd-Ag alloy degree in the fresh catalyst and subsequently in situ chlorination during the induction period of reaction. After the in situ restructuring process, the resulting Pd-Ag/nano-MgF_2 catalysts with atomically dispersed Pd sites exhibited an excellent catalytic performance for HaDHC of 1,1,1,2-tetrafluoro-2-chloropropane (HCFC-244bb) to 2,3,3,3-tetrafluoropropene (HFO-1234yf), the new-generation refrigerant, with conversion of ca. 60% and HFO-1234yf selectivity of ca. 82% at 270 °C. Characterization results reveal the Pd-Ag alloy degree in the fresh catalyst can be facilely tuned by changing the impregnation sequences for bimetallic precursors during catalysts preparation due to different metal-support interactions. Constructing a high Pd-Ag alloy degree offers a high in situ chlorination degree of catalyst surface to finally get highly isolated Pd sites. Adsorption and computational results demonstrate the chemisorbed hydrogen species on the single atom Pd sites (Pd-F and Pd-F_3 sites) boost the HFO-1234yf formation, while the spillover hydrogen species derived from the large Pd ensembles (Pd_6, Pd_7 and Pd_8 clusters) contribute to the formation of deep hydrogeneration product, 1,1,1,2-tetrafluoropropane (HFC-254eb).

Introduction

Along with the successive ratification of the Kigali amendment by various governments in recent years [1,2], it means that most of regions in the world have officially begun the phasedown of hydrofluorocarbons (HFCs), a class of potent greenhouse gases, which are used as refrigerants, blowing agents, etc., in modern societies now [3]. Therefore, for HFCs' green alternatives, much attention worldwidely is being paid on hydrofluoroolefins (HFOs) due to their similar thermophysical properties like HFCs but low impacts on environment, e.g., much lower global warming potential (GWP, <10 for HFOs) [4]. Among the HFOs, 2,3,3,3-tetrafluoropropene (HFO-1234yf), as an ideal alternative to 1,1,1,2-tetrafluoroethane (HFC-134a), is the best representative [5]. Currently, HFC-134a is the most abundantly used HFCs chemical with the global demand beyond 250 kt annually [6,7], so it has been put into the primary phaseout list by EU F-gas regulation owing to its high GWP of 1430 [4,5].

In order to obtain the -C=C- double bond, the final step for the synthesis of HFOs is almost related to the HX (X = Cl or F) elimination process of F-containing intermediates irrespective of starting materials [8,9]. For example, HFO-1234yf can be industrially synthesized by dehydrochlorination of 1,1,1,2-tetrafluoro-2-chloropropane (HCFC-244bb) or dehydrofluorination of 1,1,1,2,3-pentafluoropropane (HFC-245eb) in the vapor phase [10]. However, thermal dehydrohalogenation that is generally carried out among 600~800 °C [8] is typically a strong energy consuming process. Although using solid Lewis acid/base catalysts like F-Cr_2O_3 and SrClF can improve reaction activity to some extent [8,9], this process still has to be performed under elevated temperature due to its intrinsically endothermic feature, simultaneously suffering from low activity and fast catalyst deactivation [10]. Therefore, to fabricate a new

catalytic system capable of synthesizing efficiently HFO-1234yf under mild conditions is highly pursued so as to achieve a low-carbon full lifecycle for both the production and consumption of HFO-1234yf.

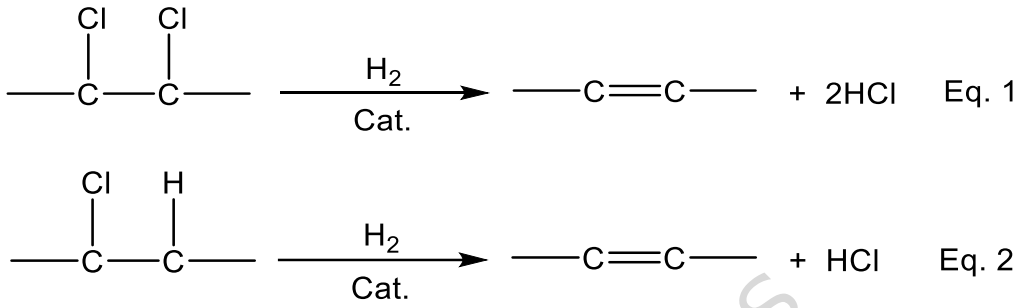

Actually, unsaturated hydrocarbons can also be formed via the dechlorination of halocarbons in the presence of H_2 over noble metal catalysts such as Pd, Pt and Ru, and transition metals such as Ni and Cu, well known as catalytic hydrogen-assisted dechlorination (CHaDC) [11-13]. Nonetheless, to our knowledge, most of earlier works pay attention on the CHaDC of vicinal chloroalkanes (two Cl atoms bond to adjacent C atoms), e.g., 1,2-dichloroethane [11] and $CF_3OCFClCF_2Cl$ [13], (Eq. 1). It is of great interests to explore whether the hydrogen-assisted dechlorination of chlorocarbons without vicinal chlorine atoms to olefins, namely, hydrogen-assisted dehydrochlorination (HaDHC), (Eq. 2) over metal catalysts is also achievable, e.g., in the case of HCFC-244bb, but which has yet to be clarified.

In the case of CHaDC, noble metals exhibit much higher activity than non-precious metals under moderate temperature (< 300 ºC), but with a poor olefin selectivity as a result of deep hydrogenation, which are generally originated in strong olefin adsorption on large noble metal ensembles [11]. To suppress hydrogenation, a bimetallic strategy is often adopted to prepare the catalyst for the selective formation of olefinic products, e.g., Pt-Cu, Pt-Sn, Pd-Ni and Pd-Ag

[11,14-17]. The addition of a secondary metal can tune the geometric properties of noble metals (dilution effect) so as to changing the adsorption of olefinic products on the catalyst surface [11,16]. Moreover, adjusting the catalyst supports and preparation methods can also modify the geometric properties of noble metals and the adsorption strength of olefinic intermediates [17,18]. Among various bimetallic catalysts, supported Pd-Ag catalysts have received much attention owing to their excellent selectivity to olefins, e.g., Ag-Pd/TiO_2 [18], Pd-Ag/Al_2O_3 [19], Ag-Pd/ZrO_2 [20], Pd-Ag/SiO_2 [21], Pd-Ag/porous carbon [22], in the CHaDC of 1,2-dichloroethane to ethylene. Based on a DFT calculation, Pd-based alloys are also predicted to display higher ethylene selectivity than Pt-based counterparts, and Ag is an efficient promoter to improve the selectivity [23]. Interestingly, in most of previous studies, the active H species formed on the catalyst surface were almost ignored as an important factor to control the product distribution. Previously, active H atoms formed on the noble metal sites were proposed to just provide the regeneration of the chlorinated metal sites like AgCl back into metallic Ag [19,21,24]. In addition, in several CHaDC of 1,2-dichloroethane to ethylene studies of supported Pd-Ag catalysts, the dilution effect of Ag has been employed to achieve the desired isolated Pd sites; however, the specific nature of the isolated Pd sites are still unclear [19,20]. More importantly, despite many efforts having been put into rational design and synthesis of metal catalysts in the CHaDC process, how to fabricate the metal-based catalysts to achieve high dehydrochlorination selectivity and inhibit the deep hydrogenation in a HaDHC process is still lack.

Recently, we showed that the HaDHC of HCFC-244bb succeeded over a Ni_3P catalyst with a rate of HFO-1234yf formation to 8.12 mmol g_{cat}^{-1} h^{-1} at 300 °C and H_2/HCFC-244bb of 1.5, and

the catalyst behavior was related to different active H species formed on the catalyst surface [25]. This finding and aforementioned results of CHaDC motivated us to assume that Pd-Ag with optimized surface H species catalyzed HaDHC of HCFC-244bb would be a promising new strategy to obtain a high HFO-1234yf yield under a more moderate temperature. Moreover, hollow nano-MgF_2 prepared by our team [26] could be an appropriate catalyst support, which is synthesized via a modified fluorolytic sol–gel method. Because it displays excellent inertness against both HCl and HF (unavoidable byproducts of organic compounds with chloro- and fluoro-groups involved reactions at elevated temperature), large surface area with mesoporous structure, and weak acidity so as to avoid the potential dehydrofluorination of HCFC-244bb and coke formation [27].

In doing so, we here report the hydrogen-assisted dehydrochlorination of HCFC-244bb over hollow nano-MgF_2 supported Pd-Ag catalysts. An induction period in the rate of HCFC-244bb conversion and HFO-1234yf selectivity was observed over the supported Pd-Ag catalysts during the initial 8 h TOS, leading to a significant enhancement in HFO-1234yf selectivity with just a little decline in catalyst activity only. A pretreatment of catalyst sample in a HCl/H_2 flow after reduction combined with microscopy and spectroscopy characterization of fresh and spent catalysts revealed that the induction period was associated with in situ chlorination of surface Pd sites during the reaction. More importantly, the introduction of Ag regulated in situ chlorination degree of surface Pd sites, rather than simply providing a dilution effect to Pd. The higher degree of Pd-Ag alloy in fresh catalysts, the heavier chlorination degree for surface Pd sites during the induction period, then leading to increased isolated and/or single-atom Pd sites. Various

adsorption/desorption results of CO/H_2/HCFC-244bb/HFO-1234yf combined with DFT calculation results manifested that the large Pd ensembles, contributing to the formation of dissociated hydrogen species desorbed at high temperature (>350 °C) ($H_{des\text{-}HT}$ species), were responsible for the occurrence of side reactions as hydrogenation; While the isolated Pd sites, contributing to the formation of the dissociated hydrogen species desorbed at low temperature (<350 °C) ($H_{des\text{-}LT}$ species), played a critical role in the catalytic HaDHC of HCFC-244bb to HFO-1234yf. During the induction period, the transformation of large Pd ensembles to sufficiently isolated Pd sites and inactive Pd^{2+} ions by a tunable in situ chlorination of Pd-Ag alloy, then leaving the Pd single-atom sites to be exposed, is responsible for increased HFO-1234yf selectivity and inhibiting deep hydrogenation. This work also provides a facile approach to precisely tailor the single-atom sites/ensemble sites heterogeneity of supported Pd catalyst via Ag mediated chlorination pretreatment.

Results

Catalytic performance of Pd-Ag/nano-MgF_2 in the HaDHC of HCFC-244bb

To evaluate how the preparation method affects the catalytic behaviors in the HaDHC of HCFC-244bb, three different nano-MgF_2 supported Pd-Ag catalysts (Pd-Ag/nano-MgF_2(P), Pd-Ag/nano-MgF_2(co) and Pd-Ag/nano-MgF_2(A)) and Pd/nano-MgF_2 were examined in a fixed bed reactor at 270 °C, H_2/HCFC-244bb molar ratio at 1:1, and contact time of 8 s. Pd-Ag/nano-MgF_2(P) means Pd precursor was firstly impregnated on nano-MgF_2 support during its preparation; and for Pd-Ag/nano-MgF_2(co), Pd and Ag precursors were together impregnated on nano-MgF_2 support during the preparation; for Pd-Ag/nano-MgF_2(A), Ag precursor was firstly impregnated on nano-

MgF_2. As shown in Figure 1A, the activity of all the catalysts progressively decreased during the initial 8 h TOS and remained steady thereafter. Based on the rate of HCFC-244bb conversion, both at the initial (after 1 h) and steady (after 8 h) period, the order of catalyst activity is as follows: Pd/nano-MgF_2 > Pd-Ag/nano-MgF_2(A) > Pd-Ag/nano-MgF_2(co) > Pd-Ag/nano-MgF_2(P), indicating the introduction of Ag undermines the activity of nano-MgF_2 supported Pd catalysts to some extent. Nonetheless, the decline of catalyst activity after the presence of Ag was not significant, which decreased slightly from 2.14 mol g_{Pd}^{-1} h^{-1} over Pd/nano-MgF_2 to 1.82 mol g_{Pd}^{-1} h^{-1} over Pd-Ag/nano-MgF_2(P) at the steady state.

Although the targeted product, HFO-1234yf was almost not observed over all the tested catalysts during the first 30 min. reaction time, its selectivity for all three nano-MgF_2 supported Pd-Ag catalysts gradually increased within the following 8 h TOS (Figure 1B). However, Pd/nano-MgF_2 maintained an extremely low selectivity to HFO-1234yf throughout reaction time. At the steady-stated conditions, Pd-Ag/nano-MgF_2(P) exhibited a highest selectivity of 82% to HFO-1234yf, followed by Pd-Ag/nano-MgF_2(co) (62%), Pd-Ag/nano-MgF_2(A) (42%) and Pd/nano-MgF_2 (~2%). It is noteworthy that the trend of HFO-1234yf selectivity at different catalysts is opposite to that of catalyst activity. Expectably, the selectivity to the secondary product 1,1,1,2-tetrafluoropropane (HFC-254eb), originated from deep hydrogenation of HFO-1234yf, showed a reversed trend compared with the observed for HFO-1234yf selectivity over all the tested catalysts (Figure 1C). Pd/nano-MgF_2 showed a stable selectivity of 82% to HFC-254eb with time on stream that was highest of all the four catalysts, while Pd-Ag/nano-MgF_2(P) showed the lowest selectivity to HFC-254eb of just 13% at steady state. In addition, minor amounts of 3,3,3-trifluoropropene

and 1,1,1-trifluoropropane as consecutive hydrodefluorination products were also detected but not discussed here. Unlike in the case of catalyst activity, the presence of Ag in nano-MgF_2 supported Pd catalysts showed a remarkably positive effect on HFO-1234yf formation based on the steady-stated results, due to suppression of side reactions, e.g., deep hydrogenation and consecutive hydrodefluorination to different extent. Moreover, the improved HFO-1234yf selectivity upon introducing Ag can precisely be tuned by different impregnation methods.

In view of the best HFO-1234yf selectivity over Pd-Ag/nano-MgF_2(P), its long-term durability was also investigated (Figure 1D), but no obvious decay in conversion and selectivity was observed within 80 h TOS. The HCFC-244bb conversion and HFO-1234yf selectivity maintained stable at ~60% and ~82% at steady state. The related rate of HFO-1234yf formation reached 7.44 mmol g_{cat}^{-1} h^{-1} over Pd-Ag/nano-MgF_2(P) at 270 °C, which is one order of magnitude higher than those obtained over CsF/MgO at 380 °C (0.32 mmol g_{cat}^{-1} h^{-1}) [27] and SrClF at 350 °C (0.16 mmol g_{cat}^{-1} h^{-1}) [28] via direct gas-phase dehydrochlorination.

With regard to the origin of the induction period, our recent work also points to an induction period over the Ni_3P catalyst in the HaDHC of HCFC-244bb due to the chlorination of catalyst surface [25]. Furthermore, some reports have suggested that the chlorination or Cl deposition of the catalyst surface by in situ generated HCl during a CHaDC process is related to this phenomenon [20,29]. To verify this point, a pretreatment of fresh Pd-Ag/nano-MgF_2(P) catalyst in a HCl/H_2 flow (50% HCl) at 175 °C for 30 min after reduction (Pd-Ag/nano-MgF_2(PC)) was carried out, and then tested in the HaDHC of HCFC-244bb at the standard conditions. The results (Figure S1) showed that no induction period appeared over Pd-Ag/nano-MgF_2(PC), but stable activity (~1.76

mol g_{Pd}^{-1} h^{-1}) and HFO-1234yf selectivity (~87%) without remarkable variation during the catalytic reaction was immediately achieved. This manifests the origin of induction period over nano-MgF_2 supported Pd-Ag catalysts can be assigned to the chlorination of catalyst surface by in situ formed HCl, thus evidencing the improvement of HFO-1234yf selectivity at the expense of a gentle decrease of activity. For comparison, conventional MgF_2 supported Pd-Ag catalysts (Pd-Ag/MgF_2(P)) comprising the same metal loadings as those of Pd-Ag/nano-MgF_2(P) were also prepared and evaluated under the same conditions. As shown in Figure S1, the steady-state HFO-1234yf selectivity over Pd-Ag/MgF_2(P) was just 60%, although the steady-state activity was 1.86 mol g_{Pd}^{-1} h^{-1}. In addition, we also measured the activity of Ag/nano-MgF_2, but the HCFC-244bb conversion was almost negligible (≤5%) under comparable conditions during the testing.

Characterization of Pd-Ag/nano-MgF_2 before and after the HaDHC of HCFC-244bb

To reveal the bulk-phase, surface local, and electronic structures of nano-MgF_2 supported Pd-Ag catalysts before and after in situ chlorination during the HaDHC process, the fresh and spent catalysts after 10 h TOS were characterized by powder X-ray diffraction (XRD), high-resolution transmission electron microscopy (HRTEM), infrared spectroscopy of CO chemisorption (CO-IR), X-ray photoelectron spectroscopy (XPS) and X-ray absorption fine structure (XAFS) spectroscopy. Moreover, the inductively coupled plasma atomic emission spectra (ICP analysis) showed that the Pd and Ag loading were 0.48~0.49 wt.% and 2.94~2.98 wt.% in four fresh catalyst samples, leading to almost the same Pd/Ag molar ratio of 1:6. XRD patterns (Figure S2A) show the presence of characteristic diffraction peaks of MgF_2 (JCPDS-72-1150) and Ag (JCPDS-89-3722) over the fresh samples but without any diffraction peaks of Pd and Pd-Ag alloy. Apart from above

diffraction peaks, the characteristic diffraction peaks of AgCl (JCPDS-85-1355) (Figure S2B) were also observed over the spent nano-MgF_2 supported Pd-Ag catalysts. This reveals that chlorination occurred on all the nano-MgF_2 supported Pd-Ag catalysts during the HaDHC of HCFC-244bb, which is in accordance with the results of catalytic performance. Moreover, as expected, the spent Pd-Ag/nano-MgF_2(P) and Pd-Ag/nano-MgF_2(PC) exhibit very similar XRD patterns. From the HRTEM images of fresh nano-MgF_2 supported Pd-Ag catalysts (Figure S3B, F and J), the lattice fringes with the calculated interlayer spacings of 0.225 and 0.231±0.001 nm, corresponding to the (111) plane of the Pd and the (111) plane of the Pd-Ag alloy [30,31], can be clearly observed. It proves the formation of monometallic Pd and Pd-Ag alloy nanoparticles in all the fresh nano-MgF_2 supported Pd-Ag catalysts. The size distribution of metal nanoparticles (Figure S3A, E and I) is centred at 18.4, 12.0 and 17.6 nm for Pd-Ag/nano-MgF_2(P), Pd-Ag/nano-MgF_2(co) and Pd-Ag/nano-MgF_2(A), respectively; while the average metal particle sizes of monometallic Pd and Ag supported catalysts are just 4.4 and 11.9 nm. This suggests the presence of both Pd and Ag on nano-MgF_2 enables the average metal particle sizes to be increased in comparison with those of monometallic samples, especially in the case of Pd-Ag/nano-MgF_2(P). Furthermore, from the high-angle annular dark-field (HAADF) images with corresponding energy-dispersive X-ray spectroscopy (EDS) elemental mapping (Figure S3C, G and K), Pd and Ag elements are uniformly dispersed in the metal particles of Pd-Ag/nano-MgF_2(P), but the homogeneous distribution of which exhibits a successively downward trend in Pd-Ag/nano-MgF_2(co) and Pd-Ag/nano-MgF_2(A). This suggests that among nano-MgF_2 supported Pd-Ag catalysts, Pd-Ag/nano-MgF_2(P) has the highest degree of alloy formation, and Pd-Ag/nano-MgF_2(A) displays the worst degree of

alloy formation. The atomic fraction of Pd/Ag in different nanoparticles determined by EDS (Figure S3D, H and L) further confirms that more Pd atoms are present in the metal particles of Pd-Ag/nano-MgF_2(P) (23.3% Pd) than in Pd-Ag/nano-MgF_2(co) (12.5% Pd) and Pd-Ag/nano-MgF_2(A) (1.2% Pd). The changes of metal particle size and elemental distribution implies that the addition of Ag into Pd/nano-MgF_2 weakens the interaction between mono-metal and nano-MgF_2 support at different level upon different alloy degrees of Pd-Ag bimetals, which in turn relies on different impregnation sequences for metal precursors during catalyst preparation.

Such an undermined interaction between bimetals and support was also evidenced by temperature programmed reduction with H_2 (H_2-TPR) analysis of the calcined nano-MgF_2 supported samples. The H_2-TPR profiles (Figure S4) show that two broad peaks around 391 and 252 °C are observed in Pd/nano-MgF_2 and Ag/nano-MgF_2, which are remarkably higher than the normal reduction temperatures of Pd (40 °C) and Ag (130 °C) [31]. Even in the case of metal oxide supported Pd with strong interaction between oxide and Pd, the reduction peak for a highly dispersed Pd species generally appears at ~200 °C [32,33]. It confirms that nano-MgF_2 has an extreme strong interaction with monometallic Pd and Ag, thus resulting in a small metal particle size in Pd/nano-MgF_2 and Ag/nano-MgF_2. However, in the bimetallic Pd-Ag catalysts, a new broad peak with two split peaks at low temperature (90~200 °C) appears and the intensity of reduction peak at high temperature (385~410 °C) decreases significantly, which is different from the linear combination of the two single-component profiles of Pd/nano-MgF_2 and Ag/nano-MgF_2. Additionally, the reduction peaks are centred at lower temperature in Pd-Ag/nano-MgF_2(P) (104 °C with a shoulder peak at 181 °C and 385 °C) than in Pd-Ag/nano-MgF_2(co) (199 °C with

a shoulder peak at 90 °C and 398 °C) and Pd-Ag/nano-MgF_2(A) (190 °C with a shoulder peak at 125 °C and 410 °C). The first peak in the range 90~104 °C is probably ascribed to the reduction of Pd-Ag precursors that are in close contact to each other, and the second peak between 180~200 °C may be assigned to the reduction of Ag precursors isolated from Pd. The third peak between 385~410 °C is attributed to the reduction of isolated Pd precursors. Moreover, quantified results (Table S1) reveal that the H_2 uptake at low temperature (< 200 °C) accounts for 87.3% of the total H_2 consumption for Pd-Ag/nano-MgF_2(P), whereas this fraction at low temperature is only 75.4% for Pd-Ag/nano-MgF_2(A). From the above analysis, we conclude that the metal-support interactions (MSIs) increase in the following order: Pd-Ag/nano-MgF_2(P) < Pd-Ag/nano-MgF_2(co) < Pd-Ag/nano-MgF_2(A) < Pd/nano-MgF_2. The weakest MSIs in Pd-Ag/nano-MgF_2(P) can be due to well dispersion of elemental Pd and Ag and intimate bimetallic structure in this sample.

HRTEM with EDS (Figure 2) was also used to examine the local structure and element distribution of spent nano-MgF_2 supported Pd-Ag catalysts and fresh Pd-Ag/nano-MgF_2(P) after treated by HCl (Pd-Ag/nano-MgF_2(PC)). The lattice fringes with the calculated interlayer spacings of 0.239, 0.277 and 0.196 nm, indexing to the (111) plane of the $PdCl_2$, and the (200) and (220) planes of the AgCl [34,35], respectively, can be observed in all the spent nano-MgF_2 supported Pd-Ag catalysts and Pd-Ag/nano-MgF_2(PC). The element mapping images further confirm the deposition of Cl on metal particles in each sample, but the Cl content in spent Pd-Ag/nano-MgF_2(co) and Pd-Ag/nano-MgF_2(A) is just half of that in spent Pd-Ag/nano-MgF_2(P). Notably, the distinct lattice fringes of Pd nanoparticles are not observed in spent Pd-Ag/nano-MgF_2(P) and

Pd-Ag/nano-MgF_2(PC), but which are still visible in spent Pd-Ag/nano-MgF_2(co) and Pd-Ag/nano-MgF_2(A).

From the Pd 3d XPS spectra (Figure 3A and Table S2), both Pd^0 ($3d_{5/2}$ peak at 334.1~334.3 eV) and Pd^{2+} ($3d_{5/2}$ peak at 336.5~337.0 eV) species are present in each fresh catalyst [36], consistent with the TEM results. The ratio of Pd^0/Pd^{2+} is in the following order: Pd-Ag/nano-MgF_2(P) (2.73) > Pd-Ag/nano-MgF_2(co) (1.99) > Pd-Ag/nano-MgF_2(A) (1.74) > Pd/nano-MgF_2 (1.52). This trend is coincidentally opposite to the order of MSIs and consistent with the order of Pd-Ag alloy degree for different catalysts, suggesting weak MSIs and high Pd-Ag alloy degree are beneficial for the reduction of Pd precursors under our experimental conditions. However, in the spent catalysts, the ratio of Pd^0/Pd^{2+} increases in the following order: Pd-Ag/nano-MgF_2(P) (0.75) < Pd-Ag/nano-MgF_2(co) (1.14) < Pd-Ag/nano-MgF_2(A) (1.29) < Pd/nano-MgF_2 (1.39). Moreover, the Cl content determined by XPS is 0.64%, 0.51%, 0.46% and 0.32% for spent Pd-Ag/nano-MgF_2(P), Pd-Ag/nano-MgF_2(co), Pd-Ag/nano-MgF_2(A) and Pd/nano-MgF_2, respectively. This means weak MSIs and high Pd-Ag alloy degree can also promote the in situ chlorination of Pd species on catalyst surface during the induction period of the reaction, which is supported by the Pd 3d XPS data of Pd-Ag/nano-MgF_2(PC). Furthermore, the surface structures and electronic states of Pd species were also investigated by CO-IR. As shown in Figure 3B, no CO adsorption is observed over fresh Ag/nano-MgF_2 and Pd/nano-MgF_2 before reduction treatment, revealing that CO is exclusively adsorbed on metallic Pd sites in the prepared catalysts. The CO adsorption bands mainly appear in the range of 2044~2063 cm^{-1} and 1947~1970 cm^{-1}, and a very weak shoulder peak at 1901 cm^{-1} can be also observed in the case of Pd-Ag/nano-MgF_2(A). The former

bands in the high wave number range belong to CO linear-bonded on isolated Pd sites, and the latter two bands in the low wave number ranges belong to CO bridge-bonded and triple-bonded on Pd clusters and nanoparticles, respectively [31,32]. Based on the integrated area of different IR bands of CO adsorbed over fresh catalysts (Table S3), the fraction of linear-bonded CO decreases in the following order: Pd-Ag/nano-MgF_2(P) (74.9%) > Pd-Ag/nano-MgF_2(co) (68.7%) > Pd-Ag/nano-MgF_2(A) (58.7%) > Pd/nano-MgF_2 (40.5%). This trend is consistent with the order of Pd-Ag alloy degree in different nano-MgF_2 supported Pd-Ag catalysts, indicating the addition of Ag and especially the Pd-Ag alloy degree strongly influence the dispersion of metallic Pd sites. Additionally, a red shift of the IR band of linear-bound CO is observed in nano-MgF_2 supported Pd-Ag catalysts compared with that in Pd/nano-MgF_2, and the biggest red shift is present in Pd-Ag/nano-MgF_2(P). This result indicates the electron transfer from Ag to Pd, and high Pd-Ag alloy degree can promote this transfer process, consistent with previous reports [18,37]. Notably, from Figure 3E and Table S3, the fraction of linear-bound CO increases significantly in all the spent catalysts. In particular, the fraction of linear-bound CO approaches 100% in spent Pd-Ag/nano-MgF_2(P) and Pd-Ag/nano-MgF_2(PC), suggesting all the metallic Pd species are present as isolated sites in these catalysts. In terms of the Pd 3d XPS and TEM results, the increase of isolated metallic Pd species in the spent catalysts can be due to the transformation of Pd clusters and nanoparticles into isolated metallic Pd sites and $PdCl_2$ via in situ chlorination during the induction period of HaDHC of HCFC-244bb. Moreover, the transition degree from Pd ensembles to isolated metallic Pd sites is associated with the alloy degree of Pd-Ag bimetal in the fresh catalysts. Indeed, considering the higher affinity of Ag sites toward C-Cl bond as compared to that of Pd sites [19],

high Pd-Ag alloy degree can provide an accessible proximity of surface Cl atoms and Pd species mediated by Ag sites, thus facilitating the in situ chlorination of Pd species resulting in the formation of more isolated metallic Pd sites. Based on the CO-IR and HRTEM results, the Pd species are mainly present as isolated sites on the spent Pd-Ag/nano-MgF_2(P), while more Pd nanoparticles with Pd-Ag alloys are present on the spent Pd-Ag/nano-MgF_2(A) and Pd-Ag/nano-MgF_2(co). Considering that the selectivity to HFO-1234yf increases in the order: Pd/nano-MgF_2 < Pd-Ag/nano-MgF_2(A) and Pd-Ag/nano-MgF_2(co) < Pd-Ag/nano-MgF_2(P), presumably, the isolated Pd sites rather Pd nanoparticles and Pd-Ag alloys favor the formation of desired product, HFO-1234yf.

To further determine the local structure of Pd sites in the spent catalysts, the normalized Pd K-edge X-ray absorption near-edge structure (XANES) spectra were taken. As shown in Figure 3C, the position of adsorption edge energy follows the order: Pd foil < Pd/nano-MgF_2 < Pd-Ag/nano-MgF_2(A) < Pd-Ag/nano-MgF_2(co) < Pd-Ag/nano-MgF_2(P) < Pd-Ag/nano-MgF_2(PC) < $PdCl_2$ < PdO, implying that the valence states of Pd in the spent catalysts are between 0 and +2. Thereinto, the valence state of Pd is enhanced from nearly 0 in spent Pd/nano-MgF_2 to nearly +2 in spent Pd-Ag/nano-MgF_2(P), being in line with the XPS data. The Fourier transforms of Pd K-edge extended X-ray absorption fine structure spectra (FT-EXAFS) (Figure 3F, Table S4 and Figure S5) reveal that as compared with standard Pd foil, $PdCl_2$ and PdO samples, two peaks at around 1.5~1.8 Å and 2.54 Å in the curve of spent Pd/nano-MgF_2 arise from the contribution of Pd−F/O/Cl bonds and contiguous Pd−Pd bonds. A upshift of the peak associated with Pd−Pd bonds to 2.65 Å is observed in spent Pd-Ag/nano-MgF_2(co) and Pd-Ag/nano-MgF_2(A), which is caused

by the presence of Pd−Ag bonds [18,38]. Moreover, as shown in Table S4, the bond distances of 2.81 and 2.82 Å for the palladium atoms to the nearest neighbors are obtained in spent Pd-Ag/nano-MgF_2(co) and Pd-Ag/nano-MgF_2(A), also indicating the formation of Pd-Ag alloy structures possessing isolated Pd atoms in an Ag matrix [39]. Only a single broad peak at 1.53 Å is observed in spent Pd-Ag/nano-MgF_2(P) and Pd-Ag/nano-MgF_2(PC), and the peak associated with Pd−Pd bonds, and the bond distance assigned to the Pd-Ag bonds are absent. In combination with the TEM and CO-IR results, this implies the atomically dispersed Pd sites on the surface of nano-MgF_2 are predominant in spent Pd-Ag/nano-MgF_2(P) and Pd-Ag/nano-MgF_2(PC). In addition, we conducted the spherical aberration-corrected transmission electron microscopy (AC-TEM) to further clarify the existence of the single Pd sites. As shown in Figure S6, the single Pd sites of Pd-Ag/nano-MgF_2(PC) were observed by AC-TEM. Considering the peak of Pd–Cl coordination for standard $PdCl_2$ at 1.84 Å, the single-atom Pd sites with the peak around 1.5 Å are basically coordinated by F/O atoms. Notably, the peak at 2.65 Å of the Pd–Pd/Ag coordination is observed in fresh Pd-Ag/nano-MgF_2(P), reinforcing our speculation that Pd sites undergo a restructuring during the induction period of HaDHC of HCFC-244bb via in situ chlorination. Specifically, large Pd clusters/nanoparticles can be partially or totally transformed into the single-atom Pd sites upon exposure to appropriately Cl-containing elevated environment, which in turn is tuned by the Pd-Ag alloy degree in the fresh nano-MgF_2 supported Pd-Ag catalysts. Based on the catalyst behavior in the HaDHC of HCFC-244bb, the selectivity to HFO-1234yf was clearly much lower over spent Pd-Ag/nano-MgF_2(co) and Pd-Ag/nano-MgF_2(A) than over spent Pd-Ag/nano-MgF_2(P) and Pd-Ag/nano-MgF_2(PC). Therefore, this implies that the formed Pd-Ag alloy on the surface of nano-

MgF_2 are not good active sites for the formation of HFO-1234yf as the single atom Pd species coordinated with F/O atoms on the surface of nano-MgF_2.

Insights on the active sites of Pd-Ag/nano-MgF_2 in the HaDHC of HCFC-244bb

To deeper understand different catalytic performances of various nano-MgF_2 supported Pd-Ag catalysts, the temperature-programmed desorption (TPD) behaviors of HFO-1234yf, HCFC-244bb and H_2 on fresh and spent catalysts were investigated. Some studies on the olefin formation via CHaDC or semi-hydrogenation have pointed out that the product distribution is closely related to the adsorption/desorption behavior of olefinic species on the Pd-based catalysts [18,40-42]. Surprisingly, from Figure S7A, the adsorption strength to HFO-1234yf is similar on spent Pd-Ag/nano-MgF_2(P), Pd-Ag/nano-MgF_2(co) and Pd-Ag/nano-MgF_2(A), as revealed by close desorption peaks in the HFO-1234yf-TPD profiles at 82, 86 and 88 ºC, respectively. The low desorption temperatures imply the adsorbed HFO-1234yf species are easily desorbed from the surface of above three catalysts. Nonetheless, spent Pd/nano-MgF_2 exhibits four HFO-1234yf desorption peaks at 87, 200, 379 and 452 ºC, indicating HFO-1234yf is prone to be strongly adsorbed on its surface. Apparently, the remarkable variation of the steady-state HFO-1234yf selectivity (from 2% to 82%) on above four catalysts in the HaDHC of HCFC-244bb cannot be primarily correlated with the affinity of catalyst surface to HFO-1234yf species. Several publications have reported that olefinic species are prone to be weakly adsorbed on the isolated Pd sites [43,44]. This means the dispersion of the Pd sites on three spent nano-MgF_2 supported Pd-Ag catalysts is capable enough to contribute to weak adsorption of HFO-1234yf on these catalysts. In addition, as shown in Figure S7A, a weak adsorption of HFO-1234yf is observed over Pd-

Ag/nano-MgF_2(P) before reduction treatment, indicating that HFO-1234yf tends to adsorb weakly on the Pd^{2+} sites. As mentioned above, the in situ chlorination of large Pd ensembles during the reaction always leads to the formation of the single-atom Pd and/or the $PdCl_2$ sites. Thus, this accounts for that regardless of the chlorine coverage, after the induction period all the nano-MgF_2 supported Pd-Ag catalysts showed a weak interaction with HFO-1234yf. Even as shown in Figure S7B, the desorption peaks of HFO-1234yf appear at different temperatures of 134, 179, 195 and 348 ºC for fresh Pd-Ag/nano-MgF_2(P), Pd-Ag/nano-MgF_2(co), Pd-Ag/nano-MgF_2(A) and Pd/nano-MgF_2, respectively. However, HFO-1234yf was almost not detected at the first 30 minutes reaction over all these catalysts, further indicating the interactions between HFO-1234yf species and nano-MgF_2 supported Pd-based catalysts do not have a decisive impact on HFO-1234yf formation. Notably, the influence of HFO-1234yf uptake of nano-MgF_2 supported Pd-based catalysts (Table S5) on HFO-1234yf selectivity cannot be excluded. Afterwards, HCFC-244bb-TPD profiles (Figure S8A and Table S6) show that the Pd sites are mainly responsible for the adsorption of HCFC-244bb, as revealed by much lower desorption temperature and HCFC-244bb uptake on Ag/nano-MgF_2 sample (T_{max} =112 ºC, $Des_{HCFC\text{-}244bb}$ = 4.3 μmol g^{-1}) than those on fresh Pd/nano-MgF_2 (T_{max} =190 ºC, $Des_{HCFC\text{-}244bb}$ = 13.1 μmol g^{-1}). Regardless of fresh or spent catalysts, Pd-Ag/nano-MgF_2(P) exhibits a highest desorption temperature and HCFC-244bb uptake, while Pd/nano-MgF_2 displays a lowest desorption temperature and HCFC-244bb uptake. The order is coincident with the trend of isolation degree of Pd sites on different nano-MgF_2 supported Pd-based catalysts determined by CO-IR, also revealing HCFC-244bb species prefer to adsorb on Pd sites. Interestingly, as shown in Figure S9, the HCFC-244bb conversion rate varies inversely with

HCFC-244bb uptake of different catalysts irrespective of fresh or spent catalysts. This implies the adsorption and activation of HCFC-244bb on the Pd sites are not the rate-determining step for the HaDHC of HCFC-244bb over nano-MgF_2 supported Pd-based catalysts. Minimizing the competitive adsorption of HCFC-244bb on the Pd sites could improve the catalyst activity.

In terms of our previous study [25], the adsorption and dissociation of hydrogen on catalyst surface are the pivotal factor for the HaDHC of HCFC-244bb process. To confirm this point, the H_2-TPD analysis of different nano-MgF_2 supported Pd-based catalysts was conducted (Figure S10 and Table S7). Two desorption zones appear in all the H_2-TPD profiles, and the desorption peak at low temperature of T_{max} in the range 150~250 ºC ($H_{des\text{-}LT}$) is generally attributed to the chemisorbed hydrogen species; while the desorption peak at high temperature of T_{max} in the range 430~530 ºC ($H_{des\text{-}HT}$) can be attributed to the spillover hydrogen species [45,46]. The hydrogen activation ability of Ag/nano-MgF_2 is almost negligible as a result of an extremely low H_2 uptake (1.7 μmol g^{-1}) on this sample. In comparison with fresh Pd/nano-MgF_2, three fresh nano-MgF_2 supported Pd-Ag catalysts exhibit lower desorption temperature and H_2 uptake, and the related trend is consistent with the order of CO uptake on various fresh nano-MgF_2 supported Pd-based catalysts. This implies the adsorption and activation of hydrogen primarily occur on the metallic Pd sites, and the interactions between H and Pd sites are weakened after introducing Ag into nano-MgF_2 supported Pd-based catalysts. Compared to fresh catalysts, the desorption peak of $H_{des\text{-}HT}$ species remarkably moves to lower temperature and the related amount of $H_{des\text{-}HT}$ species also decreases significantly in the three spent nano-MgF_2 supported Pd-Ag catalysts. However, the amount of $H_{des\text{-}LT}$ species increases to different level on above three spent catalysts, merely leading to a slight decline on the

total amount of desorbed H species in comparison with those on the fresh samples. Based on the characterization results, it can be perceived that the formation of $H_{des\text{-}HT}$ species is associated with large Pd clusters/nanoparticles, and the isolated Pd sites account for the $H_{des\text{-}LT}$ species generation. The transition from large Pd clusters/nanoparticles to isolated Pd sites during the induction period of reaction results in the above variation of hydrogen adsorption behavior on fresh and spent catalysts. Similar phenomena are also evident when comparing the related results of fresh Pd-Ag/nano-MgF_2(P) with those of Pd-Ag/nano-MgF_2(PC). More importantly, the variation of hydrogen adsorption behavior is similar to the trend of different catalytic performances. Consequently, the catalytic activity and HFO-1234yf formation rate at the steady state of reaction were correlated with the total amount of desorbed H_2 and the amount of $H_{des\text{-}LT}$ species on the spent catalysts (Figure 4B and 4C). Moreover, considering the hydrogen species are primarily adsorbed on the metallic Pd sites, the catalytic activity was also correlated with the CO uptake of different spent catalysts (Figure 4A). Obviously, there is a highly linear relationship between the catalyst activity and both total amount of desorbed H_2 and CO uptake. This reveals surface metallic Pd sites are responsible for the HaDHC of HCFC-244bb, where the adsorption and activation of hydrogen play the decisive role in reaction. Due to a strong correlation between the HFO-1234yf formation rate and the amount of $H_{des\text{-}LT}$ species, it is reasonable to speculate that the isolated and/or single-atom Pd sites enable the transformation of HCFC-244bb to HFO-1234yf. Indeed, HFO-1234yf is mainly formed on the isolated and/or single-atom Pd sites rather on Pd nanoparticles and Pd-Ag alloys based on characterization results. Conversely, as shown in Figure S11, the byproduct HFC-254eb formation rate has a highly linear relationship with the amount of

$H_{des\text{-}HT}$ species. This implies large Pd clusters/nanoparticles contributing to the strong adsorbed hydrogen species could lead to the occurrence of consecutive deep hydrogenation.

Density functional theory (DFT) calculations were also performed to reveal the functions of different Pd sites on the HFO-1234yf formation via the HaDHC process. Based on the FT-EXAFS fitting results (Table S4), the single-atom Pd sites in nano-MgF_2 supported Pd-Ag catalysts involve Pd coordination by one F/O atom and three F/O atoms, and the average coordination of the Pd ensembles is 6, 7 and 8, respectively. Besides, considering the F anion is dominant on the surface of nano-MgF_2, the exposed Pd sites on nano-MgF_2 supported Pd-based catalysts were mainly modeled as Pd−F, Pd−F_3, Pd_6, Pd_7 and Pd_8, on the MgF_2 (110) plane, respectively. As shown in Figure 5A, the calculated adsorption energies of chemisorbed hydrogen species on these Pd sites display the order of Pd−F_3(-0.59 eV) < Pd−F(-0.57 eV) < Pd_6(-0.54 eV) < Pd_7(-0.27 eV) < Pd_8(-0.20 eV). However, from Figure 5B and S12, the adsorption energies of HFO-1234yf and spillover hydrogen species show a reverse trend to the adsorption energies of chemisorbed hydrogen on different Pd sites. This suggests the highly dispersed Pd sites thermodynamically favor the activation of chemisorbed hydrogen species, while large Pd ensembles promote the generation of spillover hydrogen species and olefinic species adsorption, consistent with the H_2 and HFO-1234yf TPD results. It should be noted that the adsorption energies of HFO-1234yf vary slightly from -0.10 eV to -0.16 eV over Pd−F and Pd_6 sites, indicating the desorption behavior of olefinic species over single-atom Pd sites and small Pd clusters are similar. Furthermore, from the Gibbs free energies diagram of reaction paths for the HaDHC of HCFC-244bb (Figure 5C) [47], the elementary step involving the dehydrogenation of *CF_3-CF-CH_3 associated with another *H

resulting in the formation of *CF_3-CF=CH_2 is the rate-determining step during the initial HFO-1234yf formation process. Moreover, the free energy change of this step over Pd−F_3, Pd−F, Pd_6, Pd_7 and Pd_8 sites is -2.23, -2.05, -1.87, -1.54, and -1.18 kJ/mol, respectively. It means that the dehydrogenation of *CF_3-CF-CH_3 to *CF_3-CF=CH_2 is rather triggered by single-atom Pd sites than by Pd clusters. In addition, the elementary step involving the hydrogenation of *CF_3-CF=CH_2 with the first *H is the rate-determining step during the formation process of byproduct HFC-254eb. The Gibbs free energies change of this step over Pd−F_3, Pd−F, Pd_6, Pd_7 and Pd_8 sites is -15.53, -16.90, -23.60, -25.17 and -26.70 kJ/mol, respectively, being reverse to the order of the hydrogenation of *CF_3-CF=CH_2 on these five Pd sites. This implies the secondary hydrogenation of HFO-1234yf is more difficult on the single-atom Pd sites than on large Pd ensembles. Taking the catalytic performances and characterization of Pd-Ag/nano-MgF_2 catalysts into account, the active sites contributing to the HFO-1234yf formation are probably mainly composed of single-atom Pd sites as Pd−F_3 and Pd−F sites. The calculated binding energy of Pd-F_3 and MgF_2 is determined to be -0.54 eV. At the reaction temperature of 270 °C, the calculated free energy for the desorption process of Pd-F_3 from the MgF_2 surface is 0.28 eV, indicating that Pd-F_3 is difficult to desorb from MgF_2 [48]. Thus, the Pd-F_3-MgF_2 system exhibits an excellent stability under the reaction conditions.

Conclusions

To sum up, we report pioneeringly the successful transformation of HCFC-244bb to HFO-1234yf, the fourth generation of F-containing refrigerants via a hydrogen-assisted dehydrochlorination process under relatively mild temperature (270 °C) over nano-MgF_2 supported Pd-Ag catalyst with

atomically dispersed Pd sites. Specifically, the steady-stated HFO-1234yf formation rate over the optimal Pd-Ag/nano-MgF_2 catalysts is 23.2 times and 46.5 times higher than those over the reported CsF/MgO and SrClF catalysts via gas-phase direct dehydrochlorination. Changing the impregnation sequences for bimetallic precursors in catalysts preparation can finely tune the alloy degree for various fresh Pd-Ag/nano-MgF_2 catalysts, finally resulting in different restructuring of Pd sites for these catalysts via in situ chlorination during the induction period of the reaction. More isolated and/or single-atom Pd sites are formed originating from the in situ chlorination of large Pd ensembles, which is mediated by alloy degree of Pd-Ag in the fresh catalysts. Although all the fresh catalysts are not effective for the HFO-1234yf formation, the increased isolated and/or single-atom Pd sites formation due to an in situ restructuring process greatly enhances the selectivity to HFO-1234yf (from ~0% to >80%). The catalyst activity and product distribution are primarily determined by the adsorption and activation of hydrogen rather than due to adsorption of olefinic species over Pd sites. The more adsorbed hydrogen species on the single-atom Pd sites, the higher the HFO-1234yf formation rate. In contrast, the generation of spillover hydrogen species derived from large Pd ensembles leads to the consecutive formation of byproduct of deep hydrogenation. Our work for the first time offers insights into the hydrogen-assisted dehydrochlorination over nano metal fluoride supported Pd catalysts, and opens the path to a powerful and facile strategy for designing catalysts with tunable isolated Pd sites and high olefin selectivity.

Methods

Synthesis of nano-MgF_2

Magnesium nitrate hexahydrate ($Mg(NO_3)_2 \cdot 6H_2O$, 99.9%) and polyethylene glycol (PEG2000)

were dissolved in ethylene glycol (EG) under stirring at 60 °C, with the Mg^{2+} concentration fixing at 0.5 M and the PEG2000/EG mass ratio of 1:10. Then, an aqueous solution of hydrogen fluoride (40 wt.%) was introduced stepwise into the mixture under vigorous stirring over 6 h, maintaining a Mg/F molar ratio of 1:4. The resulting transparent and colorless sol was aged overnight at room temperature and then transferred to an oven at 90 °C for 24 h to form a transparent wet gel. The gel was dried at 150 °C for 8 h to obtain a white gel powder. This powder was subsequently calcined in air using a muffle furnace at 400 °C for 5 h, yielding to obtain the nano-MgF_2 with a surface area of 97.9 m^2 g^{-1} [26]. For comparison, the classic MgF_2 was prepared by fluorinating an aqueous slurry of $MgCO_3$ with hydrofluoric acid (40 wt.%) (Mg concentration = 1.0 M, molar ratio of Mg/F = 1:4), followed by filtration, drying and final calcination at 400 °C in air for 5 h (S_{BET} = 44.2 m^2 g^{-1}).

Catalysts preparation

Two incipient wetness impregnation approaches including stepwise and co-impregnation were utilized to prepare hollow nano-MgF_2 supported Pd-Ag bimetallic catalysts. Typically, 5 g of nano-MgF_2 powder was added into an acetone solution of palladium(II) acetate with a given amount of Pd (0.5 wt.%), followed by drying in an oven at 90 °C for 10 h and subsequently calcination in static air at 325 °C for 4 h. Afterwards, the resulting solid was added into an aqueous solution of silver nitrate with a given amount of Ag (3.0 wt.%), then dried in an oven at 90 °C for 10 h and subsequently calcined in static air at 300 °C for 2 h, resulting in a catalyst denoted as Pd-Ag/nano-MgF_2(P). For comparison, another Pd-Ag/nano-MgF_2 catalyst denoted as Pd-Ag/nano-MgF_2(A) was prepared by a reverse impregnation sequence to that for Pd-Ag/nano-MgF_2 catalysts. In detail,

the nano-MgF_2 powder was firstly impregnated by an aqueous solution of silver nitrate, following by drying at 90 °C for 10 h and calcination at 300 °C for 2 h. Then, the recovered solid was impregnated by an acetone solution of palladium(II) acetate, following by dried at 90 °C for 10 h and calcined at 325 °C for 4 h. In addition, Pd-Ag/nano-MgF_2 catalysts were also prepared via co-impregnation of nano-MgF_2 powder by a mixture of acetone solution of palladium(II) acetate and aqueous solution of silver nitrate followed by drying at 90 °C for 10 h and calcination at 325 °C for 4 h (denoted as Pd-Ag/nano-MgF_2(co)).

The Pd-Ag supported on the classic MgF_2 catalyst (denoted as Pd-Ag/MgF_2(P)) was also prepared, and the preparation procedure was the same as that for Pd-Ag/nano-MgF_2(P). A Pd/nano-MgF_2 with the given Pd loading of 0.5 wt.% and a Ag/nano-MgF_2 with the given Ag loading of 3.0 wt.% were also prepared via the similar procedure for the nano-MgF_2 supported Pd-Ag bimetallic catalyst.

A reduction process was carried out for all the prepared catalysts before reaction. The pelletized sample with a size of 40~60 mesh was activated in a flow of H_2 under atmosphere pressure at 325 °C for 2 h to obtain the final catalyst. Furthermore, in some cases, the reduced Pd-Ag/nano-MgF_2(P) was also pretreated by a flow of HCl (20 mL min^{-1}) and H_2 (20 mL min^{-1}) mixture at 175 °C for 30 min, which was denoted as Pd-Ag/nano-MgF_2(PC).

Catalytic activity

All the catalytic reactions for HaDHC of HCFC-244bb (98.6% HCFC-244bb, provided by Xi'an Modern Chemistry Research Institute) were carried out under atmospheric pressure in a fixed bed stainless steel reactor (62 cm length with 10 mm inner diameter). Typically, all fresh catalysts were

pelleted, crushed, and sieved to 40–60 mesh that enabled the elimination of transport limitations. Prior to reaction, 3 mL (about 1.6-1.9 g) of pelletized catalyst without dilution was held at the center of the stainless steel reactor and firstly reduced in a flow of H_2 (20 mL min^{-1}) under atmosphere pressure at 325 °C for 2 h. In case of pretreatment, the reduced catalysts were cooled down to 175 °C in H_2 atmosphere, then pretreated by a flow of HCl/H_2 mixture (HCl/H_2=1:1). This was followed by flowing the reactant mixture H_2 and HCFC-244bb at the same temperature (270°) over the catalyst. The contact time (C.T.) was fixed at 8.0 s and the molar ratio of H_2 and HCFC-244bb was 1:1. The H_2 flow was monitored using a Sevenstar mass flow controller (D-07), and HCFC-244bb was delivered by a high-pressure constant flow pump (ELITE, P230II) and preheated in a vaporizer at 200 °C before being fed into the reactor. All pipes were electrically heated and maintained at 60 °C to avoid condensation of HCFC-244bb as well as any other products. The reactor effluent was passed through an aqueous solution of KOH to trap acid gases like HCl and HF, subsequently analyzed by an Agilent 7890 gas chromatograph equipped with a flame ionization detector, employing a GS-GASPRO capillary column (60 m ×0.32 mm).

Catalysts characterization

For ex situ characterization, the fresh catalyst samples were firstly reduced under a H_2 atmosphere at 325 °C for 120 min before characterization. The spent catalysts and the catalysts pretreated by a flow of HCl/H_2 were directly removed from the reactor for characterization. XRD data was characterized using an Empyrean, PANalytical X-ray diffractometer with Cu Ka radiation (k = 1.540 Å) at room temperature. The diffraction patterns were collected from 5 to 90° with a step of 0.02°. XPS was used to analyze the change of the coordination state of surface element measured

by Thermo Scientific ESCALAB Xi+ equipment. The binding energy values were calibrated against the C 1s signal (BE = 284.8 eV) of contaminant carbon. Images and EDS data were collected with a JEOL JEM-2100F instrument in transmission electron microscopy (TEM) mode. The sample was first ground and diluted in ethanol. A drop of the suspension was then deposited on a carbon film. The morphology and particle size, EDS elemental linear scan and elemental mapping of the nanoparticles were characterized at 200 kV. AC-STEM analysis was performed on a JEOL-JEM-ARM300F microscope with a spherical aberration corrector. The XAFS spectra of the Pd K edge were characterized at the synchrotron radiation facility BL14W1 in Shanghai, China. The Pd K-edge XANES data were collected in fluorescence mode. Pd foil, $PdCl_2$ and PdO samples were used for comparison. EXAFS data were processed by using the Athena and Artemis modules in the Demeter software package. The loading of Pd and Ag was tested by inductively coupled plasma optical emission spectrometer (ICP-OES) on an Aglient 5110 spectrometer.

The CO chemisorption was measured on the AutoChem II 2920. For fresh sample, 0.15 g sample after calcination was reduced under a H_2/Ar flow (50 mL min^{-1} flow rate, heating from 20 to 325 °C at a rate of 10 °C min^{-1}, and then holding at 325 °C for 120 min). After cooling to 30 °C under Ar, CO adsorption started. CO loop gas was used for each pulse, and several pulses were introduced until saturation. The amount of CO was measured with a thermal conductivity detector (TCD). For spent sample and the sample pretreated by a flow of HCl/H_2, before the measurement, the sample was treated by purging under an Ar flow at 200 °C for 60 min. After cooling to 30 °C under Ar, the treatment followed the same procedures as CO adsorption as described fresh sample.

Temperature programmed reduction (H_2-TPR) measurements were performed on the same

instrument as for CO chemisorption. Before the measurement, the samples were pretreated in a He flow at 150 °C for 60 min. After cooling to 50 °C under He, the gas was switched to H_2/Ar and the sample bed was heated to 600 °C at a ramp of 10 °C min^{-1}. The consumption of H_2 was determined by TCD.

In situ Fourier transform infrared (FTIR) spectra of CO adsorption was recorded using a VERTEX 80v FT-IR spectrometer. Before CO adsorption, the samples after calcination were firstly reduced at 325 °C for 120 min in H_2/Ar (30 mL min^{-1}) and then cooled to room temperature. The background spectra were collected in a continuous Ar flow. CO adsorption was carried out in a flow of 10 vol.% CO/He (30 mL min^{-1}) for 30 min, followed by purging under N_2 atmosphere (30 mL min^{-1}) for 30 min. Finally, the spectra were collected. For spent sample and the sample pretreated by a flow of HCl/H_2, before the measurement, the sample was treated by purging under an Ar flow at 200 °C for 60 min. After cooling to 30 °C under Ar, the treatment followed the procedures as describes for the CO-IR of fresh samples.

The temperature-programmed desorption of hydrogen (H_2-TPD) measurements were performed on the same instrument as for CO chemisorption. For fresh samples, before the measurement, 0.15 g sample was reduced under H_2/Ar at 325 °C for 120 min. After cooling to 50 °C, the sample was treated in the H_2/Ar atmosphere in a flow rate of 50 mL min^{-1} for 30 min. After that, sample was purged under Ar for 30 min, followed by heating up to 650 °C at a rate of 10 °C min^{-1} in He. For spent samples and the samples pretreated by a flow of HCl/H_2, prior to measurement, they were purged under an Ar flow at 200 °C for 60 min. After cooling to 50 °C under Ar, the same procedures as described for H_2-TPD of fresh sample was employed. The HCFC-

244bb-TPD and HFO-1234yf-TPD were measured by the same procedure as described for H_2-TPD.

DFT calculations

All structural optimizations and energy calculations were based on Density Functional Theory (DFT) utilizing the VASP software package. Core and valence electron characteristics were described using the Projector-Augmented Wave (PAW) method with a cutoff energy of 500 eV, combined with Perdew Burke Ernzerhof (PBE) exchange-correction functional [49-51]. Brillouin zone sampling was carried out through a 2 × 2 × 1 Gamma-centered Monkhorst-Pack *k* grid [52]. A 15 Å vacuum layer was used to avoid interactions between two periodic units [53]. Structural optimization was deemed complete when both atomic energies and forces reached thresholds of 10^{-6} eV and 0.05 eV/Å, respectively. All the configuration were visualized and analyzed by VESTA [54].

From experimental observations, a simplified computational model of Pd single atom and Pd clusters on the MgF_2(110) surface were employed. The MgF_2 (110) surface was modeled with a (6 × 3) supercell of a (110) slab cleaved from tetragonal MgF_2. The vacuum region above the surface was set to a width of 15 Å. The adsorption energy ($E_{ads, M}$) was defined as $E_{ads, M} = E_{*M} - E_{*} - E_{M, g}$, where E_{*M}, E_{*}, and $E_{M, g}$ represent the total energy of adsorption configurations containing the surface and molecules (*M, M = CH_2=CF-CF_3 and H_2), the computational model surface (*), and molecules in the gas phase (M, g), respectively.

Author contributions

Chen Yang: Investigation, Methodology and Experiments. **Wei Mao:** Conception, Resources,

Methodology and Writing - Reviewing & Editing. **Xingzong Dong:** Formal analysis. **Song Tian:** Formal analysis. **Jinni Shen:** DFT calculation. **Zhaotie Liu:** Writing - Review & Editing and Funding acquisition. **Wei Zhang:** Writing - Review & Editing and Funding acquisition. **Jian Lu:** Writing - Review & Editing and Funding acquisition. **Erhard Kemnitz:** Writing - Review & Editing.

Declaration of Competing Interest

The authors declare that they have no known competing financial interests or personal relationships that could have appeared to influence the work reported in this paper.

Data availability

The data that support the findings of this study are available from the corresponding author upon request. The raw data for the theoretical calculations during this study are included in Supplementary Data 1 file. All the raw data for the figures during this study are included in Supplementary Data 2 file.

Acknowledgements

We are grateful to be financially supported by Central-guided local Sci-Tech Development Fund (No. 2022ZY2-JCYJ-02), Smart Gird-National Science and Technology Major Project of China (No. 2025ZD0807500), Basic Research Program in Natural Science of Shanxi Province (No. 2025JC-YBQN-216, 2025SYS-SYSZD-017). Erhard Kemnitz is dedicating this paper to Prof. Dr. Christian Limberg on occasion of his 60th birthday.

References

[1] Wang, J. et al. Potential reduction in emissions after replacement of automobile air conditioning

refrigerants in China. *Energy Rep*. **8**, 141-151 (2022).

[2] Thomson, J. D. et al. Fluoroform (CHF_3) production from CF_3CHO photolysis and implications for the decomposition of hydrofluoroolefins and hydrochlorofluoroolefins in the atmosphere. *J. Am. Chem. Soc*. **147**, 33-38 (2024).

[3] Omclinden, M. et al. Limited options for low-global-warming-potential refrigerants. *Nat. Commun*. **8**, 14476 (2017).

[4] Mclinden, M. O., Seeton, C. J. & Pearson. A. New refrigerants and system configurations for vapor-compression refrigeration. *Science* **370**, 791-796 (2020).

[5] van Renssen, S. The greenhouse-gas gang. *Nat. Clim. Change*. **2**, 143-144 (2012).

[6] Zhang, J.-J. & Wang, C. China's hydrofluorocarbon challenge. *Nat. Clim. Change*. **4**, 943-945 (2014).

[7] Dreveton, A. Overview of the fluorochemicals industrial sectors. *Procedia Eng*. **138**, 240-247 (2016).

[8] Sicard, A. J.& Baker, R. T. Fluorocarbon refrigerants and their syntheses: Past to present. *Chem. Rev*. **120**, 9164-9303 (2020).

[9] Bellabarba, R. M. Catalysts for modern fluorinated refrigerants. *J. Fluorine Chem*. **244**, 109741 (2021).

[10] Nappa, M., Peng, S. & Sun, X. Industrial syntheses of hydrohaloolefins and related products. *Mod. Synth. Processes React. Fluorinated Compd.* Elsevier, 2017, pp. 27-69.

[11] Kovalchuk, V. I. & d'Itri, J. L. Catalytic chemistry of chloro- and chlorofluorocarbon dehalogenation: from macroscopic observations to molecular level understanding. *Appl. Catal. A*

271, 13-25 (2004).

[12] Śrębowata, A. et al. Remarkable effect of post synthesis preparation procedures on catalytic properties of Ni-loaded BEA zeolites in hydrodechlorination of 1,2-dichloroethane. *Appl. Catal. B* **147**, 208-220 (2014).

[13] Gregori, M. et al. Hydrogen-assisted dechlorination of $CF_3OCFCl\text{-}CF_2Cl$ to $CF_3OCF{=}CF_2$ over different metal-supported catalysts. *Appl. Catal. A* **470**, 123-131 (2014).

[14] Śrębowata, A. et al. Hydrodechlorination of 1,2-dichloroethane on active carbon supported palladium-nickel catalysts. *Catal. Today*. **124**, 28-35 (2007).

[15] Śrębowata, A. et al. Hydrogen-assisted dechlorination of 1,2-dichloroethane on active carbon supported palladium-copper catalysts. *Catal. Today*. **175**, 576-584 (2011).

[16] Xu L, et al. Mechanistic study of 1,2-dichloroethane hydrodechlorination on Cu-rich Pt-Cu alloys: Combining reaction kinetics experiments with DFT calculations and microkinetic modeling. *ACS Sustainable Chem. Eng*. **10**, 1509-1523 (2022).

[17] Wei, X. et al. Synthesis of $Pt\text{-}Cu/SiO_2$ catalysts with different structures and their application in hydrodechlorination of 1,2-dichloroethane. *Appl. Catal. B* **121-122**, 105-114 (2012).

[18] Ball, M. R. et al. Hydrodechlorination of 1,2-dichloroethane on supported AgPd catalysts. *J. Catal*. **370**, 241-250 (2019).

[19] Sun, J.-Y. et al. Selective hydrodechlorination of 1,2-dichloroethane catalyzed by trace Pd decorated Ag/Al_2O_3 catalysts prepared by galvanic replacement. *Appl. Surf. Sci*. **428**, 703-709 (2018).

[20] Han, Y.-X. et al. Highly selective hydrodechlorination of 1,2-dichloroethane to ethylene over

Ag-Pd/ZrO_2 catalysts with trace Pd. *Appl. Catal. A* **519**, 1-6 (2016).

[21] Lambert, S. et al. Pd-Ag/SiO_2 and Pd-Cu/SiO_2 cogelled xerogel catalysts for selective hydrodechlorination of 1,2-dichloroethane into ethylene. *Catal. Today*. **100**, 283-289 (2005).

[22] Job, N. et al. Hydrodechlorination of 1,2-dichloroethane on Pd-Ag catalysts supported on tailored texture carbon xerogels. *Catal. Today*. **102-103**, 234-241 (2005).

[23] Xu, L., Stangland, E. E. & Mavrikakis. M. Ethylene versus ethane: a DFT-based selectivity descriptor for efficient catalyst screening. *J. Catal*. **362**, 18-24 (2018).

[24] Heinrichs, B., Schoebrechts, J. P. & Pirard, J. P. Palladium-silver sol-gel catalysts for selective hydrodechlorination of 1,2-dichloroethane into ethylene. III. Kinetics and reaction mechanism. *J. Catal*. **200**, 309–320 (2001).

[25] Tian, S. et al. Breakthrough synthesis of 2,3,3,3-tetrafluoropropene via hydrogen assisted selective dehydrochlorination of 1,1,1,2-tetrafluoro-2-chloropropane over nickel phosphides. *J. Catal*. **391**, 366-377 (2020).

[26] Jia, Z.-H. et al. Hollow nano-MgF_2 supported catalysts: Highly active and stable in gas-phase dehydrofluorination of 1,1,1,3,3-pentafluoropropane. *Appl. Catal. B* **238**, 599-608 (2018).

[27] Mao, W. et al. Highly selective dehydrochlorination of 1,1,1,2-tetrafluoro-2-chloropropane to 2,3,3,3-tetrafluoropropeneover alkali metal fluoride modified MgO catalysts. *ChemCatChem*. **9**, 824-832 (2017).

[28] Teinz, K. et al. Catalytic formation of 2,3,3,3-tetrafluoropropene from 2-chloro-3,3,3-trifluoropropene at fluorinated chromia: A study ofreaction pathways. *Appl. Catal. B* **165**, 200-208 (2015).

[29] Early, K. O. et al. Hydrogen-assisted 1,2,3-trichloropropane dechlorination on supported Pt-Sn catalysts. *Appl. Catal. B* **26**, 257-263 (2000).

[30] Li, X. et al. Constructing a highly active Pd atomically dispersed catalyst for cinnamaldehyde hydrogenation: Synergistic catalysis between Pd-N_3 single Atoms and fully exposed Pd clusters. *ACS Catal*. **14**, 2369-2379 (2024).

[31] Miao, C.-L. et al. Array modified molded alumina supported PdAg catalyst for selective acetylene hydrogenation: Intrinsic kinetics enhancement and thermal effect optimization. *Ind. Eng. Chem. Res*. **60**, 8362-8374 (2021).

[32] Muravev, V. et al. Size of cerium dioxide support nanocrystals dictates reactivity of highly dispersed palladium catalysts. *Science* **380**, 1174-1178 (2023).

[33] Li, Z.-W. et al. Decoupling active sites enables low-temperature semihydrogenation of acetylene. *ACS Catal*. **14**, 1514-1524 (2024).

[34] Mottaghi, N. et al. Ag/Pd core-shell nanoparticles by a successive method: Pulsed laser ablation of Ag in water and reduction reaction of $PdCl_2$. *Appl. Surf. Sci*. **292**, 892-897 (2014).

[35] Singh, K. B. et al. Sonication-assisted synthesis of Ag@AgCl and Ag@AgCl-GO and their photocatalytic performances. *J. Mol. Struct*. **1269**, 133756 (2022).

[36] Hu, Z.-X. et al. High-rate and selective C_2H_6- to -C_2H_4 photodehydrogenation enabled by partially oxidized $Pd^{\delta+}$ species anchored on ZnO nanosheets under mild conditions. *J. Am. Chem. Soc*. **146**, 16490-16498 (2024).

[37] Yang, Y. et al. Breaking scaling relationships in alkynol semihydrogenation by manipulating

interstitial atoms in Pd with d-electron gain. *Nat. Commun*. **13**, 2754 (2022).

[38] Mori, K. et al. Surface engineering of a supported PdAg catalyst for hydrogenation of CO_2 to formic acid: Elucidating the active Pd atoms in alloy nanoparticles. *J. Am. Chem. Soc*. **140**, 8902-8909 (2018).

[39] Aich, P. et al. Single-atom alloy Pd–Ag catalyst for selective hydrogenation of acrolein. *J. Phys. Chem. C* **119**, 18140-18148 (2015).

[40] Cao, Y.-Q. et al. Selective hydrogenation of acetylene over Pd-In/Al_2O_3 catalyst: promotional effect of indium and composition-dependent performance. *ACS Catal*. **7**, 7835-7846 (2017).

[41] Bai, R.-S. et al. Encapsulation of palladium carbide subnanometric species in zeolite boosts highly selective semihydrogenation of alkynes. *Angew. Chem. Int. Ed.* **62**, e202313101 (2023).

[42] Zou, S.-H. et al. Grafting nanometer metal/oxide interface towards enhanced low-temperature acetylene semihydrogenation. *Nat. Commun*. **12**, 5770 (2021).

[43] Yang, T.-X. et al. Improvement of selectivity in acetylene hydrogenation with comparable activity over ordered PdCu catalysts induced by posttreatment. *ACS Appl. Mater. Interfaces*. **13**, 706-716 (2021).

[44] Xu, X.-J. et al. Thermal effect optimization endows a selective and stable PdCu single atom alloy catalyst for acetylene hydrogenation. *AIChE J*. **69**, e18042 (2023).

[45] Amorim, C. & Keane, M. A. Catalytic hydrodechlorination of chloroaromatic gas streams promoted by Pd and Ni: The role of hydrogen spillover. J. *Hazard. Mater*. **211-212**, 208-217 (2012).

[46] Sun, M.-S. et al. N-containing silane coupling agent-assisted synthesis of highly dispersed and stable PdC phase for semi-hydrogenation of acetylene. *Chem. Eng. Sci.* **247**, 116939 (2022).

[47] Simone, E. D. et al. Decoding the role of adsorbates entropy in the reactivity of single-atom catalysts. *ACS Catal*. **15**, 447-456 (2025).

[48] Saptal, V. B. et al. An adaptive palladium single-atom catalyst enabling reactivity switching between borylation and C−C coupling. *J. Am. Chem. Soc*. **147**, 18524-18540 (2025).

[49] Kresse, G. & Hafner, J. Ab initio molecular dynamics for liquid metals. Phys. Rev. B 47, 558-561 (1993).

[50] Kresse, G. & Furthmüller, J. Efficiency of ab-initio total energy calculations for metals and semiconductors using a plane-wave basis set. Comput. Mater. Sci. 6, 15-50 (1996).

[51] Blöchl, P. E. Projector augmented-wave method. Phys. Rev B 50, 17953-17979 (1994).

[52] Perdew, J. P., Burke, K. & Ernzerhof, M. Generalized gradient approximation made simple. Phys. Rev. Lett. 77, 3865-3868. (1996).

[53] Pack, J. D. & Monkhorst, H. J. "Special points for Brillouin-zone integrations"-a reply. Phys. Rev. B 16, 1748-1749 (1977).

[54] Momma, K & Izumi, F. VESTA 3 for three-dimensional visualization of crystal, volumetric and morphology data. J. Appl. Crystallogr. 44, 1272-1276 (2011).

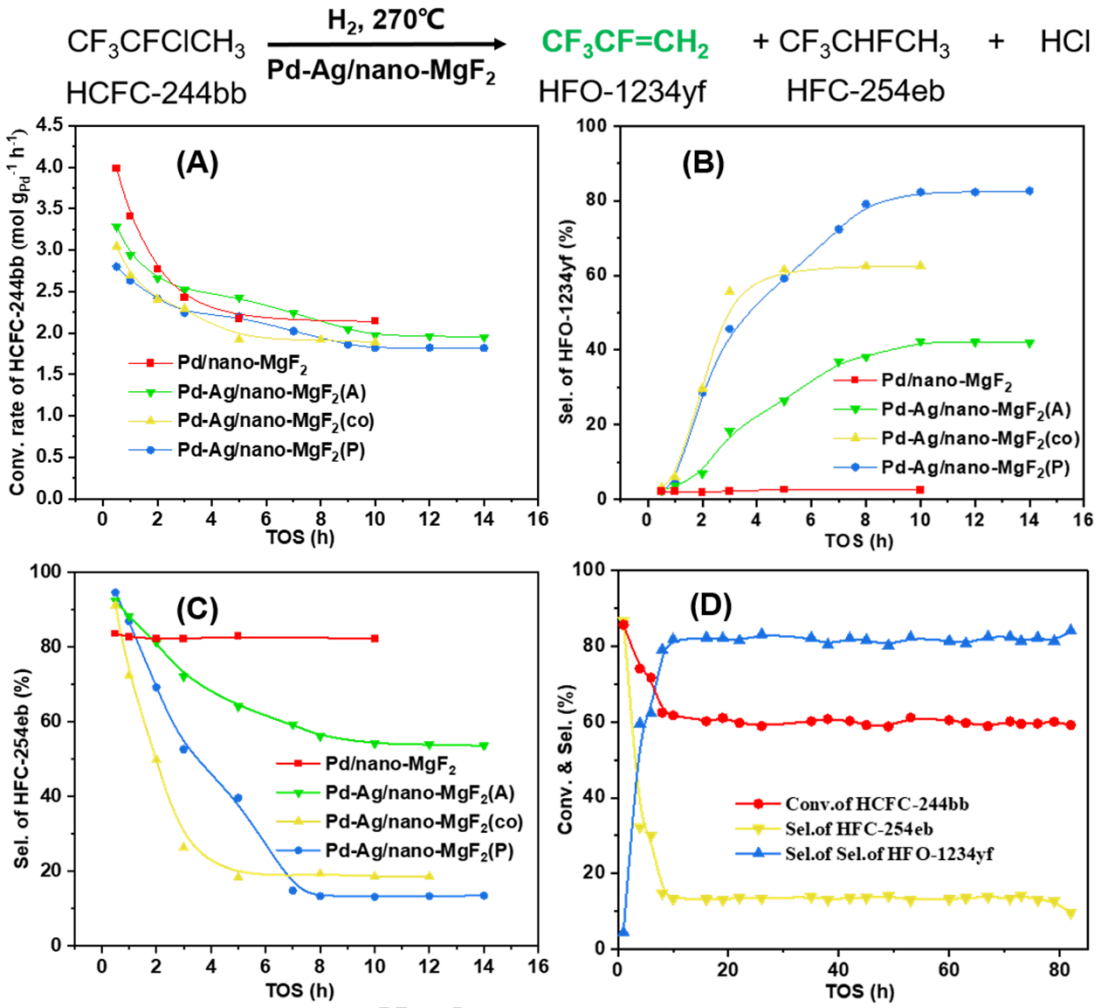

Figure 1 Catalytic performances of nano-MgF_2 supported Pd-Ag catalysts in the H_2-assisted dehydrochlorination of HCFC-244bb. (A) HCFC-244bb conversion rate, (B) HFO-1234yf selectivity, and (C) HFC-254eb (1,1,1,2-tetrafluoropropane) selectivity as a function of time over different catalysts; (D) Long-term catalytic stability of Pd-Ag/nano-MgF_2(P). Reaction condition: H_2/HCFC-244bb = 1:1, contact time = 8 s, atmospheric pressure, 270 °C.

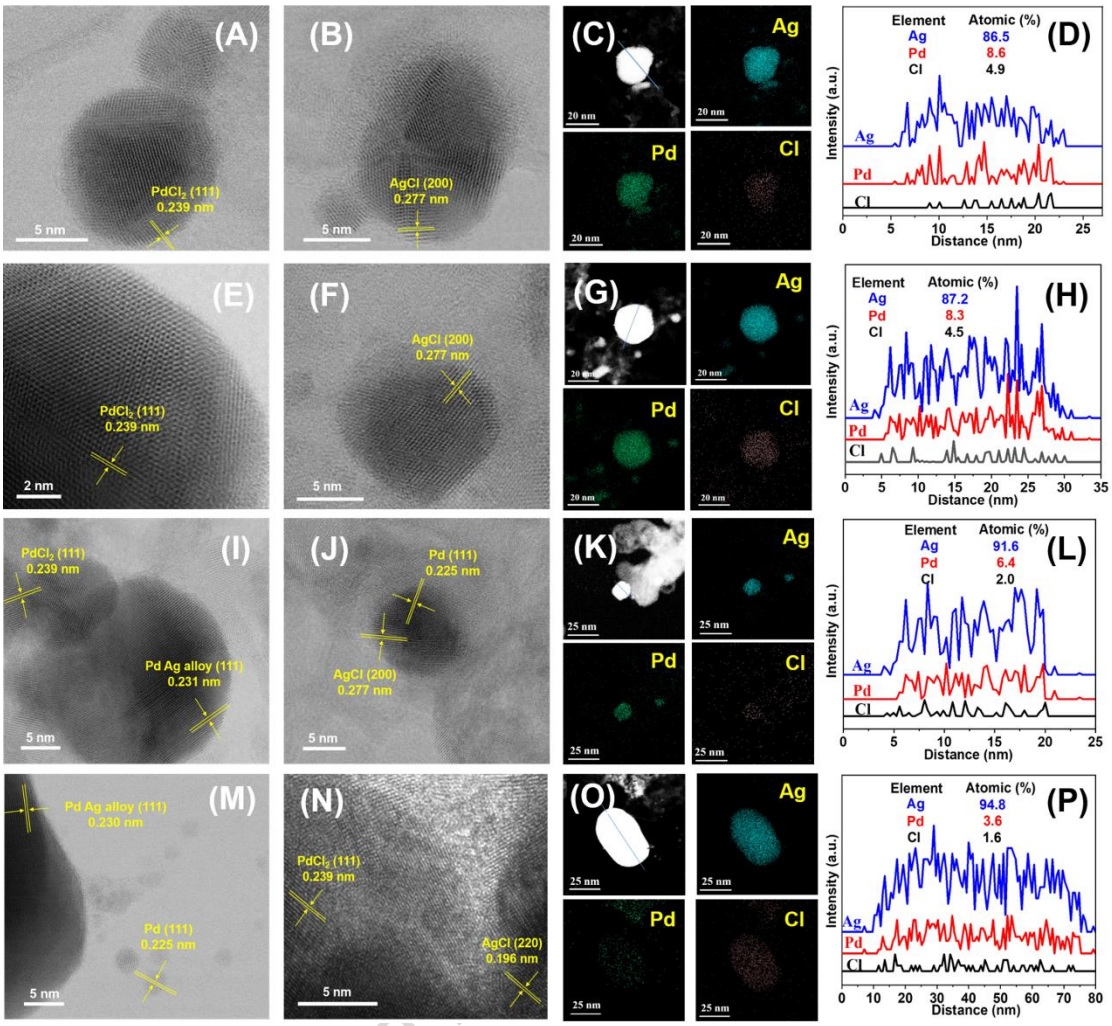

Figure 2 HRTEM images and HAADF images with corresponding EDS elemental mapping and line scanning of spent nano-MgF_2 supported Pd-Ag catalysts and fresh Pd-Ag/nano-MgF_2(P) after treated by HCl. (A-D) Pd-Ag/nano-MgF_2(PC), (E-H) spent Pd-Ag/nano-MgF_2(P), (I-L) spent Pd-Ag/nano-MgF_2(co), and (M-P) spent Pd-Ag/nano-MgF_2(A).

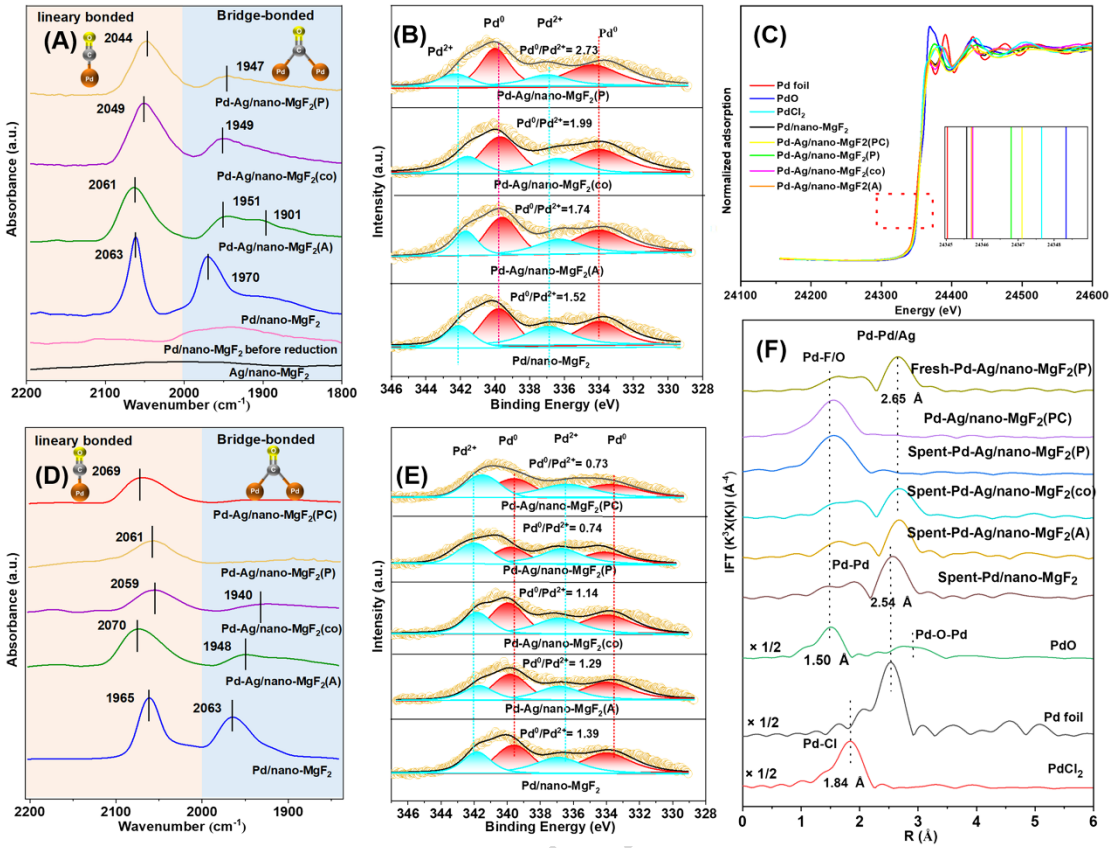

Figure 3 Electronic properties of nano-MgF_2 supported Pd-Ag catalysts before and after reaction. (A) Fresh and (D) Spent catalysts for CO-IR, (B) Fresh and (E) Spent catalysts for Pd 3d XPS spectra, (C) Normalized Pd K-edge XANES spectra and (F) Fourier-transformed k^3-weighted spectra of Pd K-edge EXAFS for spent catalysts and reference samples.

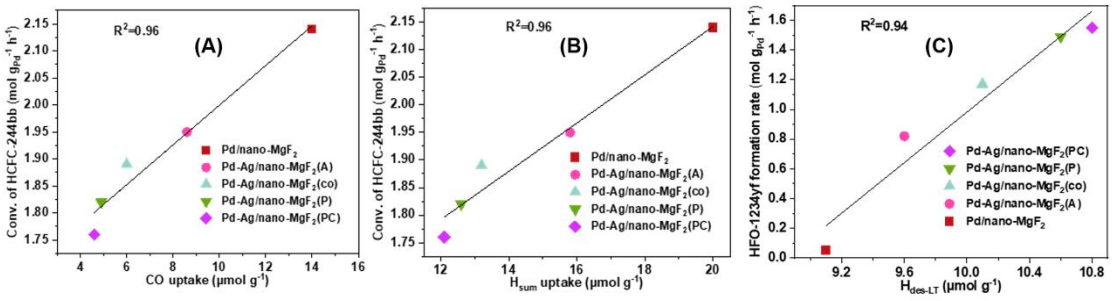

Figure 4 Relationship between catalytic performance and CO/H_2 uptake. (A) CO uptake and (B) total amount of desorbed H_2 of different spent catalysts and Pd-Ag/nano-MgF_2(PC), and (C) HFO-1234yf formation rate as a function of the amount of $H_{des\text{-}LT}$ species on the spent catalysts and Pd-Ag/nano-MgF_2(PC).

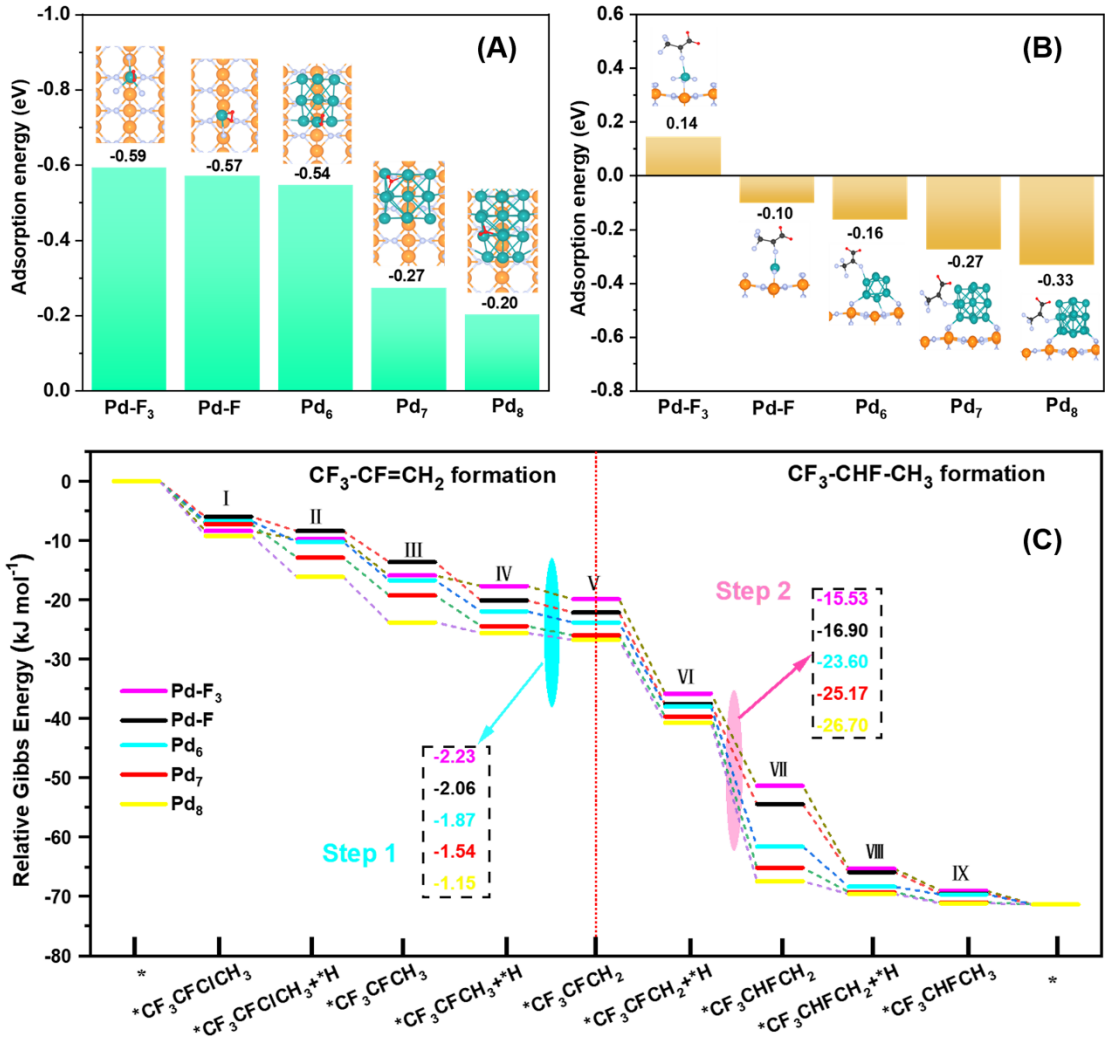

Figure 5 DFT calculations for the HaDHC of HCFC-244bb to HFO-1234yf over nano-MgF2 supported Pd-Ag catalysts. (A) adsorption energies of chemisorbed hydrogen species, (B) adsorption energies of HFO-1234yf, and (C) Relative Gibbs energy diagram of reaction pathway on various Pd sites.

Editor summary:

Hydrogen-assisted dehydrochlorination (HaDHC) is an attractive route for the production of fluorine-containing olefins under relatively mild conditions, but highly efficient metal-based catalysts for this reaction remain underexplored. Here, the authors report a nano-MgF_2 supported Pd-Ag catalyst with tunable Pd dispersion that is optimized by tuning of the Pd-Ag alloy degree in the fresh catalyst followed by in situ restructuring, and demonstrate its performance in the HaDHC of 1,1,1,2-tetrafluoro-2-chloropropane (HCFC-244bb) to 2,3,3,3-tetrafluoropropene (HFO-1234yf), a hydrofluoroolefin refrigerant with reduced global warming impact.

Peer-review information:

Communications Chemistry thanks the anonymous reviewers for their contribution to the peer review of this work.

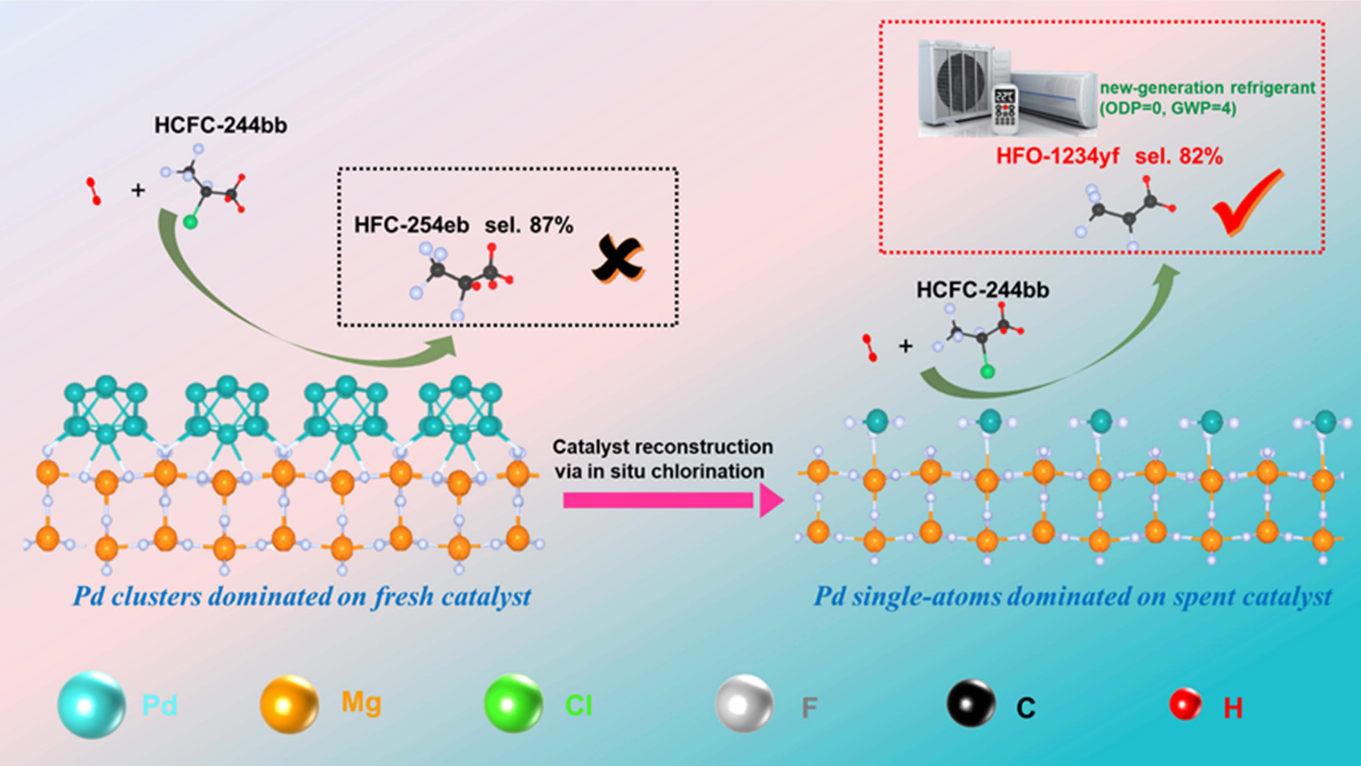
HCFC-244bb
HFC-254eb sel. 87%
new-generation refrigerant
(ODP=0, GWP=4)
HFO-1234yf sel. 82%
HCFC-244bb
Catalyst reconstruction
via in situ chlorination
Pd clusters dominated on fresh catalyst
Pd single-atoms dominated on spent catalyst
Pd
Mg
Cl
F
C
H